Fabrication of aluminum/stainless steel bimetallic composites through a combination of additive manufacturing and vacuum-assisted melt infiltration casting

M. Ghasri-Khouzani[1], X. Li[1], A.A. Bogno[2], Z. Chen[1], J. Liu[2], H. Henein[2], A.J. Qureshi[1*]

[1] Department of Mechanical Engineering, University of Alberta, Edmonton, AB T6G 1H9, Canada

[2] Department of Chemical and Materials Engineering, University of Alberta, Edmonton, AB T6G 1H9, Canada

(* Corresponding author. Email: ajquresh@ualberta.ca)

Abstract

This paper provides a hybrid method for net shape, lattice based, complex bimetallic composites using a combination of laser powder bed additive manufacturing and vacuum-assisted melt infiltration casting process. 316L stainless steel lattice structures were built using a selective laser melting (SLM) technique. Then, their cavities were filled with an aluminum alloy using vacuum-assisted melt infiltration to yield a bimetallic composite. For comparison purposes, monolithic aluminum alloy was also cast under the same casting parameters. Tensile properties of the fabricated stainless steel lattice and bimetallic composite were found to be insignificantly different. This was explained by the observed continuous gap in the 316L stainless steel/aluminum alloy interfaces which prevented load transfer from the stainless steel lattice to the aluminum matrix during tension. However, compressive properties of the bimetallic composite were found to be

significantly greater than those of the stainless steel lattice implying that the aluminum alloy matrix plays an important role during compressive deformation of the bimetallic composites. The monolithic aluminum alloy sample exhibited a noticeably higher elastic modulus, yield stress and ultimate tensile strength but a dramatically lower elongation than both the steel lattice and bimetallic composite specimen. Detachment of the stainless steel lattice from the aluminum matrix was determined to be the root cause of failure for the bimetallic composite in tension.

Keywords: selective laser melting; melt infiltration casting; bimetallic composite; mechanical properties; fractography

1. Introduction

Metal additive manufacturing (MAM), also called metal 3D printing, has become popular in recent years owing to its capability to fabricate parts with complex geometry directly from computer-aided design (CAD). The principle of MAM uses a "bottom-up" approach of material deposition from powder/wire feedstock. Many MAM techniques have been developed in the last two decades, which can be categorized based on heat source type, nature of feedstock material, and layering mechanism. The powder bed fusion (PBF) category of MAM has been the subject of numerous studies. The category includes selective laser melting (SLM) [1], – also termed direct metal laser sintering (DMLS) [2], electron beam melting (EBM) [3], and selective laser sintering (SLS) [4] processes. In these techniques, a focused laser or electron beam is used to selectively melt a thin layer of metal powder which is uniformly spread on a flat build plate. Upon local melting of one

layer, another thin metal powder layer is spread on top of the previously deposited metal. The beam is then activated on this new surface and the presence of layering powder and activating the beam is repeated until a 3D object is built. The present study specifically focuses on the SLM technique which offers better dimensional precision, higher spatial resolution, and greater material flexibility compared to other MAM techniques [5, 6]. The method has been used for a variety of metallic materials including titanium alloys [7, 8], aluminum alloys [9–11], nickel alloys [12–14], and steels [15–19].

Bimetallic composites are a type of metal matrix composites consisting of two different metallic alloys where the transition from one alloy to another can be gradual or sudden. The bimetallic composites can exhibit superior thermal and mechanical properties as well as high corrosion resistance required for marine, aerospace, nuclear and tooling industries. These materials were initially produced through welding dissimilar metals. Fabrication of Al/Cu bimetallic composite by cold rolled welding [20], Inconel 625/plain carbon steel by explosion welding [21], and Cu/steel by laser welding [22] are some examples. Another conventional technique to fabricate bimetallic composite is casting. Viala et al. [23] manufactured automotive suspension parts consisting of an Al-Si alloy and cast iron insert by a gravity die casting. In another study, Vendra et al. [24] used a simple gravity casting to fabricate aluminum/steel bimetallic composites. Recently, MAM has also been used to fabricate bimetallic composites. The most common MAM technology for this application is powder-based direct energy deposition (DED), in which transition from one metal to another is made conveniently by altering the powder feedstock. Various bimetallic composites such as Inconel 625/Cu [25], Ti/steel [26, 27], Cu/steel [28], and Ni/steel [29] were built by this technique. However, the relatively low resolution associated with DED limits application of this method for parts with complex geometries. SLM is another MAM technique which was shown to

be capable of manufacturing bimetallic composites. For example, Liu et al. [30] successfully fabricated bimetallic laminates of 316L stainless steel and C18400 copper alloy using SLM. They observed a good metallurgical bond between two metals [30]. Fe/Al–12Si bimetallic composites were also built using a novel SLM platform enabling controlled and gradual deposition of layers with different chemical composition [31]. In another study, Mei et al. [32] manufactured bimetallic composites of 316L stainless steel and Inconel 718 using SLM. However, they observed some cracks and holes at or near the interfaces [32]. SLM fabrication of Ti/stainless steel composites through a copper alloy interlayer has also been reported [33]. However, it should be noted that converting the original SLM system to composite manufacturing one is much more complicated compared to the DED system.

Despite SLM being capable of building near net shape bimetallic composites [30–33], the relatively low production rate of this technique is a drawback. The objective of the present study is to combine SLM with casting to improve the productivity. In bimetallic composite design, the component with complex geometry can be fabricated by SLM where the simple geometry component is built by casting. A practical example is high heat flux applications where the design comprises copper cooling channels and nickel superalloy blocks [25, 34, 35]. In the present study, 316L stainless steel lattice structures were built using the SLM technique. Then, a molten aluminum alloy infiltrated the cavities of the 316L stainless steel lattice to yield the bimetallic composite. Finally, mechanical properties, microstructure, and fracture behavior of the fabricated materials were analyzed thoroughly.

2. Experimental Procedure

2.1. SLM process

The feedstock material for the SLM process was argon-atomized 316L stainless steel powder with a particle size range of 15-45 μm. The chemical composition of the powder is listed in Table 1. Diamond lattice structure parts (Fig. 1(b,c)) were fabricated using an EOS M290 machine, equipped with an Yb-fiber laser. Diamond lattice structure was selected in this study because it was anticipated to exhibit higher stiffness than other lattice structures with the same density [36]. The parts had two different geometries: one for compressive testing and one for tensile testing (see Fig. 1(b,c)). The compressive sample (Fig. 1(b)) was a cube with a side of 12.5 mm. The tensile sample (Fig. 1(c)), however, had a dog-bone geometry whose dimensions conformed to ASTM E8M standard (gauge length of 50 mm and gauge width of 12.5 mm) [37]. To achieve reliable tensile properties, the failure needs to occur in gauge zone. Indeed, the failure must not take place in the interfaces between the lattice zone and solid zone, where stress concentration existed. Thus, some fillets were added to these interfaces in both ends of the tensile specimens as shown in Fig. 1(c). The tensile specimens were fabricated in a horizontal orientation with respect to the build plate, which was a hot-rolled mild steel panel with dimensions of 252 mm × 252 mm × 25 mm. The optimized process parameters for the 316L stainless steel recommended by EOS Company were employed including 20 μm powder layer thickness, 195 W laser power, 1083 mm/s scan speed, and 80 μm hatch spacing. All the lattice parts were built using an alternating scan pattern, where the hatching direction of each layer was rotated by 67° from that of the previous one. To maintain the oxygen level in the build chamber less than 0.1 %, an ultra-high purity argon gas was purged into it during the fabrication process. The build plate temperature was kept at 80 ºC to reduce stresses imposed by thermal cycles.

Table 1. Chemical composition of 316L stainless steel powder used as the feedstock material for the AM process (wt. %).

C	Cr	Mn	Mo	N	Ni	O	S	Si	Fe
0.03	17.9	2.0	2.4	0.1	13.9	0.04	0.01	0.75	Balance

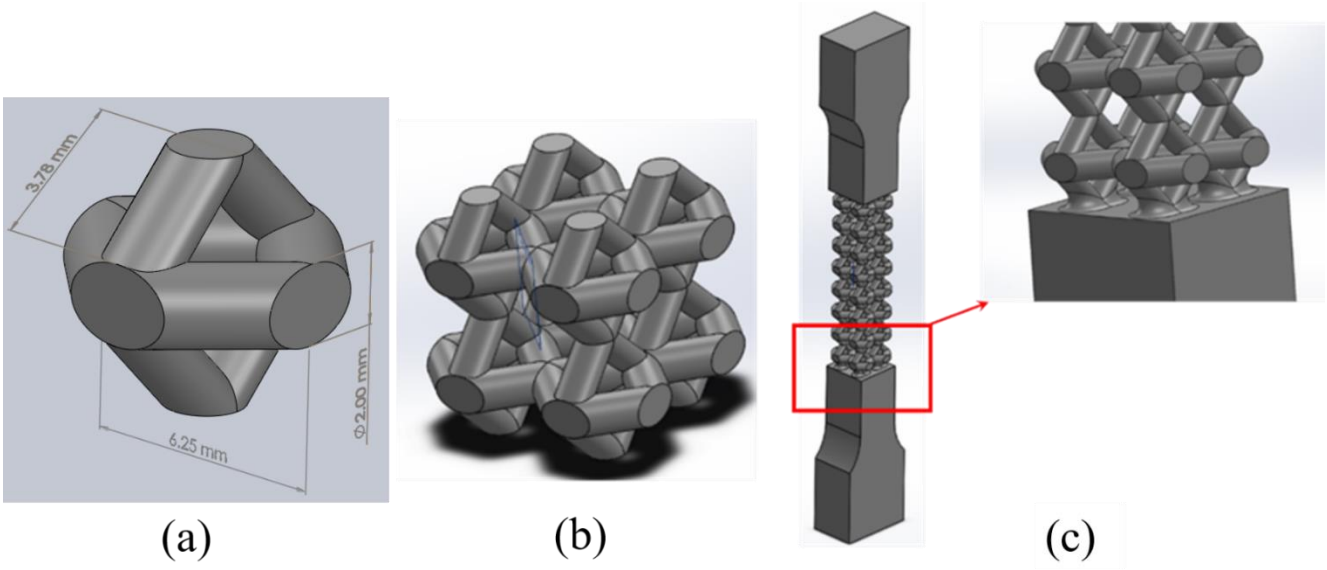

Fig. 1. (a) Unit cell dimensions of the diamond lattice structure selected in the present study; (b) compressive and (c) tensile testing specimen with the diamond lattice structure fabricated by SLM.

2.2. Casting process

The chemical composition of the aluminum alloy used for the casting process is listed in Table 2. This special aluminum alloy can be a good candidate for dissolvable tool applications due to its high corrosion rate and mechanical properties. The presence of Ag and Ga accelerates the corrosion rate, whereas Mg and Cu enhance the mechanical properties of the aluminum alloy. The SLM fabricated stainless steel lattices were covered with a 2 mm-thick wax shell. To make a plaster mold, a commercial investment powder (Plasticast BANDUST) was mixed with water

under the powder/water weight ratio of 0.4. The slurry was then poured into a flask containing the stainless steel lattices. The presence of the wax shell on the lattice structures prevented the penetration of the slurry into the lattice cavities. To ensure that the flask was properly filled with slurry, it was exposed to a vacuum (10^{-5} Pa) for 90 seconds. After hardening of the slurry at room temperature, it was heated up to 732 °C to dissipate the wax, dehydrate the mold, and eliminate residual carbon followed by furnace cooling to room temperature.

The plaster mold containing the stainless steel lattices was pre-heated to 250 °C, and held for an hour in an oven. In the meantime, the aluminum alloy feedstock was placed in a graphite crucible, heated up to 850 ˚C and held for 1 hour in an electrical furnace. When the heating regime of the mold containing the stainless steel lattices was completed, it was placed on a vacuum table. Finally, the molten aluminum alloy with the superheat temperature of 850 ˚C was immediately cast into the plaster mold and infiltrated the 316L stainless steel lattice cavities under the vacuum to yield the bimetallic composite parts. The relatively high pouring temperature (850 ˚C) was used to enhance the fluidability the molten aluminum. To better explain the microstructure and mechanical behavior of the bimetallic composites, monolithic aluminum parts (with no stainless steels) were also cast under the same conditions. An image of all experimental samples in this study is illustrated in Fig. 2.

Table 2. The chemical composition of the aluminum alloy used for casting (wt. %).

Fe	Ag	Ga	Cu	Mg	Al
0.6	2.1	2.0	2.6	4.1	Balance

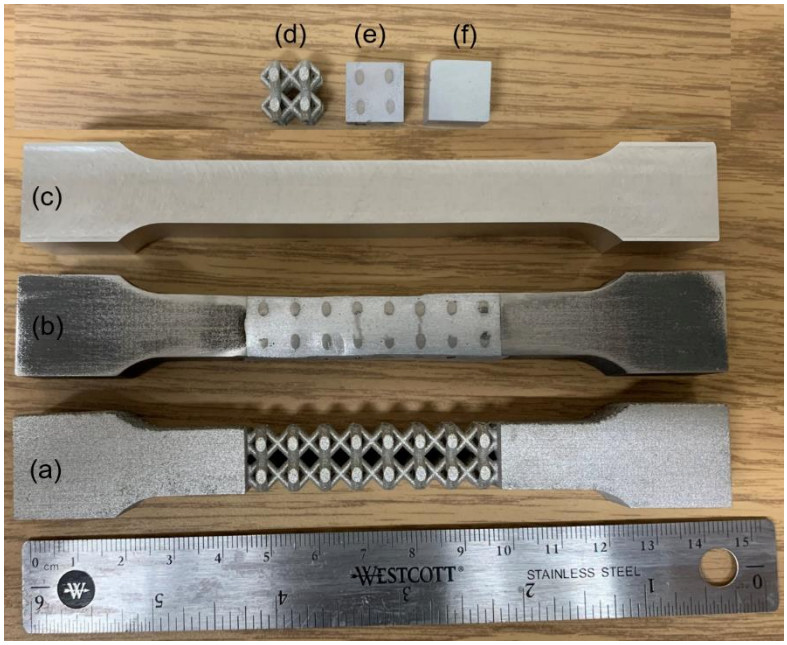

Fig. 2. An image of the experimental samples: (a) stainless steel lattice dog-bone; (b) stainless steel/aluminum composite dog-bone; (c) monolithic aluminum dog-bone; (d) stainless steel lattice cube; (e) stainless steel/aluminum composite cube; (f) monolithic aluminum cube. The cubes and dog-bones were used for compressive and tensile tests, respectively.

2.3. Microstructural analysis

For microstructural characterization, bimetallic composites were cross-sectioned followed by grinding with SiC papers, polishing with diamond suspension, and polishing with colloidal silica down to a 0.05 μm finish. Then, the samples were ultrasonically cleaned in acetone for 15 minutes. Microstructural observation and compositional analyses were performed using a TESCAN VEGA3 scanning electron microscope (SEM) coupled with an energy dispersive spectrometer (EDS) under accelerating voltages of 20 kV and a working distance of 15 mm. The EDS data was collected and analyzed using Oxford Aztec 3.0 software.

2.4. Mechanical testing

Room temperature uniaxial tensile and compressive tests were performed on all the experimental materials (316L stainless steel lattice, monolithic aluminum alloy, and 316L stainless steel lattice/aluminum alloy bimetallic composite). The compressive testing specimen was a cube with a side of 12.5 mm. The tensile testing specimen, however, had a dog-bone geometry whose dimensions conformed to ASTM E8M standard (gauge length of 50 mm and gauge width of 12.5 mm) [37]. All the tests were conducted in a displacement-controlled mode using a servo-hydraulic mechanical testing system (MTS 810). The cross-head speed was 0.5 mm/min for compressive tests and 2.0 mm/min for tensile tests. The tensile tests went to fracture whereas the compressive tests went until the maximum load limit of the mechanical testing frame (100 kN). In the case of the tensile tests, the specimen elongation was monitored using a standard strain gauge extensometer with a 50 mm gauge length. Fractographic analysis on the fractured surfaces of the tensile specimens was also carried out using TESCAN VEGA3 SEM at an operating voltage of 20 kV and a working distance of 10 mm.

3. Results and Discussion

3.1. Microstructural characterization

SEM-EDS was used to examine the 316L stainless steel lattice/aluminum alloy interfaces in the fabricated bimetallic composites. Fig. 3 illustrates the SEM micrographs from the interface at two different magnifications. A continuous gap was observed in the interface region. The formation of the gap can be attributed to the dramatically higher thermal conductivity of the aluminum compared to steel. This leads to a higher cooling rate of aluminum than steel, and therefore,

residual stresses in the interfaces. Gap formation in the steel/aluminum interfaces of the bimetallic composites have also been reported in other studies [23, 38].

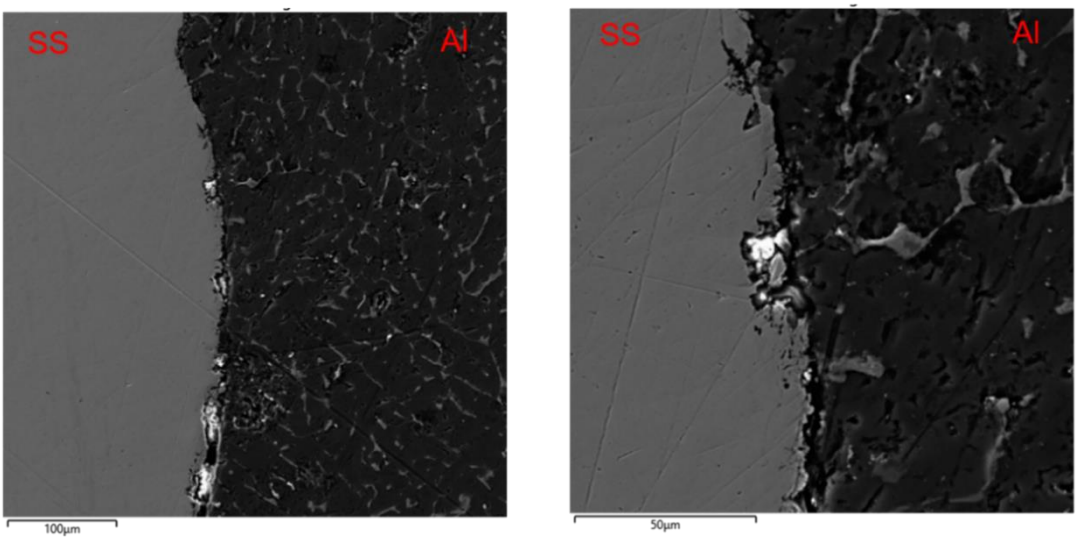

Fig. 3. SEM micrographs from the 316L stainless steel/aluminum alloy interface at two different magnifications.

EDS elemental maps from the 316L stainless steel lattice/aluminum alloy interface are presented in Fig. 4. No intermetallic compounds were observed in the interface, which can be explained by the relatively high solidification rate in addition to absence of Si in the chemical composition of the aluminum alloy. The formation, shape, size, and distribution of intermetallics in the aluminum/steel interfaces are highly dependent on the processing temperature, chemical composition, and nature of contact between steel and aluminum [24]. Vendra et al. [24] observed three intermetallic compounds ($FeAl_4Si$, Fe_2Al_7Si, and $Fe_{25}Al_{60}Si_{15}$) in the steel/aluminum interfaces, where Si was present in all three phases.

Further inspection of Fig. 4 reveals the accumulation of both Cu and Mg in the aluminum grain boundaries. Since these two alloying elements enhance the aluminum strength by solid solution

strengthening mechanism, their accumulation in the grain boundaries is not favored. By contrast, the distribution of both Cr and Ni in the stainless steel was uniform. This shows an important advantage of the additive manufacturing over casting, which is uniform distribution of alloying elements. Indeed, the extremely high solidification rate associated with SLM does not allow the alloying elements to segregate [39, 40].

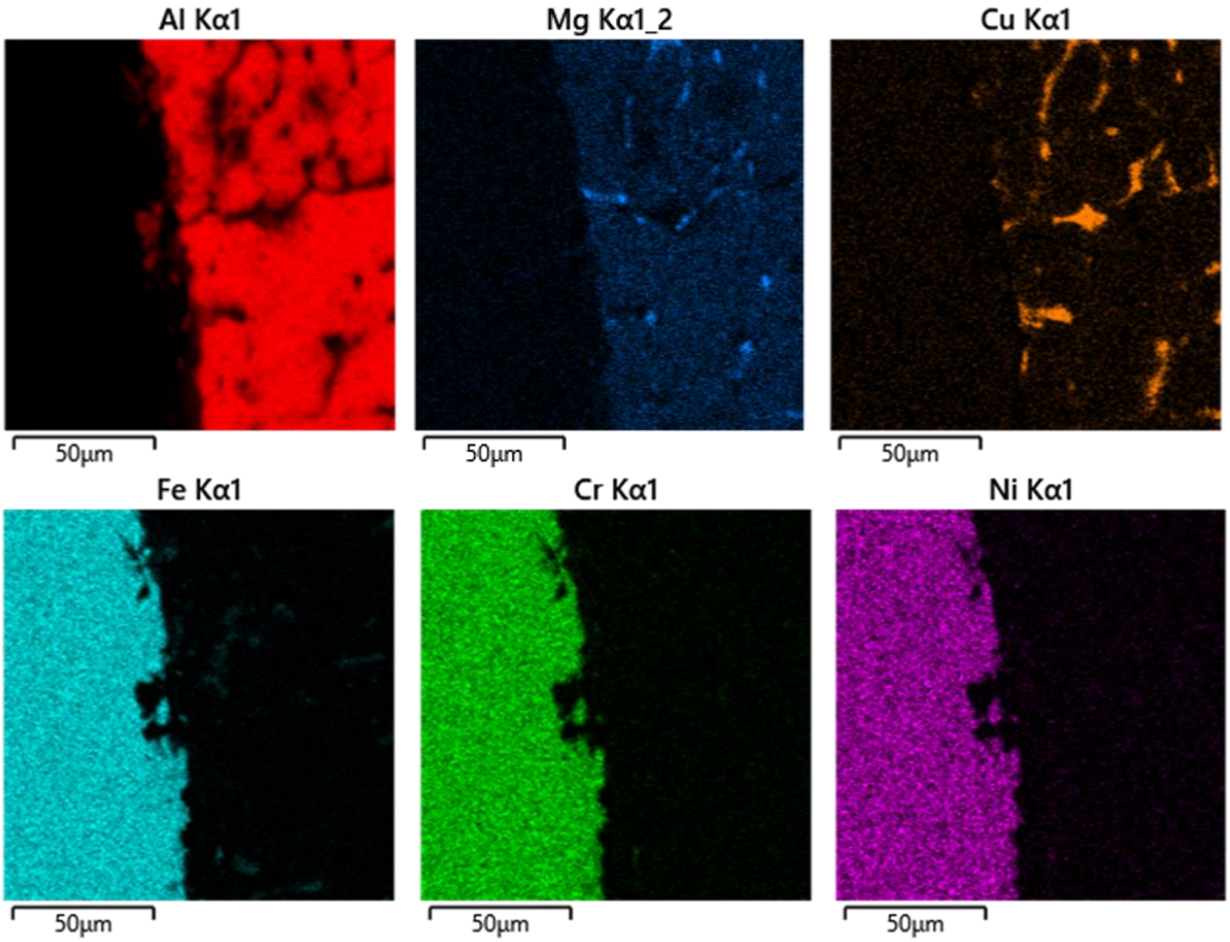

Fig. 4. EDS elemental maps from the 316L stainless steel/aluminum alloy interface.

The pore volume fraction of the SLM fabricated 316L stainless steel lattice and as-cast monolithic aluminum alloy was measured using pycnometry to be 1.1 % and 6.4 %, respectively. The high porosity content of the as-cast monolithic aluminum alloy is attributed to the relatively high

superheat temperature (850 °C) applied during casting. In fact, the amount of dissolved gases in the melt (and thus gas porosity) increase when the melt pouring temperature rises [41, 42]

3.2. Tensile behavior evaluation

Representative room temperature engineering strain-engineering stress curves for tensile behavior of all experimental materials are plotted in Fig. 5. Summary tensile characteristics derived from these curves are listed in Table 3. For all experimental materials, yield stress was determined using 0.002 strain offset method. Moreover, work hardening coefficient was determined by Hollomon equation. It is evident from Fig. 5 that all tensile curves exhibited continuous yielding. However, the tensile plot for the bimetallic composite exhibited some dips in the plastic region which can be attributed to the discontinuous microstructure of this material. From Fig. 5, it can be seen that the tensile curves for the stainless steel lattice and bimetallic composite were insignificantly different. This indicates that the aluminum matrix does not play an important role during tensile deformation of the bimetallic composite. In other words, the presence of the continuous gaps in the 316L stainless steel/aluminum alloy interfaces prevents load transfer from the stainless steel lattice to the aluminum matrix. It is worth noting that for both the stainless steel lattice and bimetallic composite specimens, the average cross sectional area of the lattice (60.99 mm^2) was used for stress calculations. This means that the load-displacement plots for these two specimens were also similar. It is evident from Fig. 5 that the tensile behavior of the monolithic aluminum alloy was dramatically different from that of the 316L stainless steel lattice and 316L stainless steel/aluminum composite.

The monolithic alloy exhibited a significantly higher elastic modulus, yield stress and UTS but a noticeably lower elongation than bimetallic composite specimen (see Fig. 5). By contrast, an Al/steel bimetallic composite fabricated by accumulative roll bonding was reported to have a higher yield stress and elongation but lower elongation than monolithic aluminum owing to strengthening effect of steel reinforcement layers [43]. A similar trend was also observed for the SLM fabricated Al/steel bimetallic composite due to formation of FeAl intermetallic compounds [31]. However, Al/steel bimetallic composites fabricated by laser fusion brazing were found to have a lower strength than the monolithic aluminum alloy [44]. In a similar study, tensile strength of an Al/steel bimetallic composite fabricated by friction stir welding was found to be lower than that of monolithic aluminum due to formation of intermetallic compounds [45]. Acarer et al. [46] reported that yield stress, UTS, and elongation of explosive welded Al/steel bimetallic composites were greater than those of the monolithic aluminum alloy. Comparing the mechanical property results of this research with the ones from literature [43–46] indicates that those fabrication techniques that result in a strong metallurgical bond between aluminum and steel will lead to bimetallic composites with excellent mechanical properties. This is a challenge because aluminum and steel are incompatible owing to their different thermo-physical properties. Moreover, formation of intermetallic compounds in the Al/steel interfaces is often associated with a high strength but poor ductility [31].

It can be seen from Table 3 that the UTS and elongation of the 316L stainless steel lattice with a relative density of 28.8 % were 147 MPa and 22 %, respectively. Given the cross-sectional area of 60.99 mm^2, the ultimate tensile force can be calculated to be approximately 9.0 kN. The ultimate tensile force and elongation for an f2cc,z 316L stainless steel lattice with a relative density of 33 % was reported to be 20.7 kN and 5.8 %, respectively [47]. The difference in mechanical properties

can be attributed to the difference in the lattice design, relative density, and SLM process parameters. By considering both ultimate tensile force and elongation, it can be concluded that the diamond lattice used in the present study can be a better candidate for energy absorption purposes compared to the f2cc,z lattice. Bulk (nonporous) 316L stainless steel fabricated by SLM was reported to exhibit a yield stress and UTS of 539 MPa and 644 MPa, respectively [48] as listed in Table 3. Thus, the 316L stainless steel lattice with a relative density of 28.8 % in this study was expected to have a yield stress and UTS of 155 MPa and 185 MPa, respectively. These values are 46 % and 21 % higher than the yield stress and UTS experimentally measured for the 316L stainless steel lattice (see Table 3). The differences can be explained by the exposure of the stainless steel lattice to the burnout cycle (heating up to 732 ˚C) in this study. In a similar study, Shamsujjoha et al. [49] observed a 42 % drop in yield stress and a 15 % decrease in UTS upon annealing the SLM fabricated 316L stainless steel. They attributed the lower yield stress and UTS of the annealed steel to its larger grain size and lower dislocation density compared to the as-built steel [49].

The elastic modulus of the monolithic aluminum alloy was measured to be 33 GPa, as listed in Table 3. Since this alloy is a special one, there was not any studies on its mechanical properties in the literature. However, the elastic modulus of the as-cast A356 aluminum alloy was reported to be 40 GPa [50], which is comparable with 33 GPa measured in the present study. In the case of stainless steel lattice with a relative density of 28.8 %, the elastic modulus was measured to be 21 GPa (see Table 3). Kohnen et al. [47] reported even a lower elastic modulus (11 GPa) for a 316L stainless steel lattice with a relative density of 33 %. Thus, the lower elastic modulus of the stainless steel lattice than that of a bulk (nonporous) aluminum alloy was observed in the present study and was also interpreted from the data in literature. This is not surprising considering the

significant presence of cavities (approximately 70 vol. %) in the structure of the stainless steel lattice.

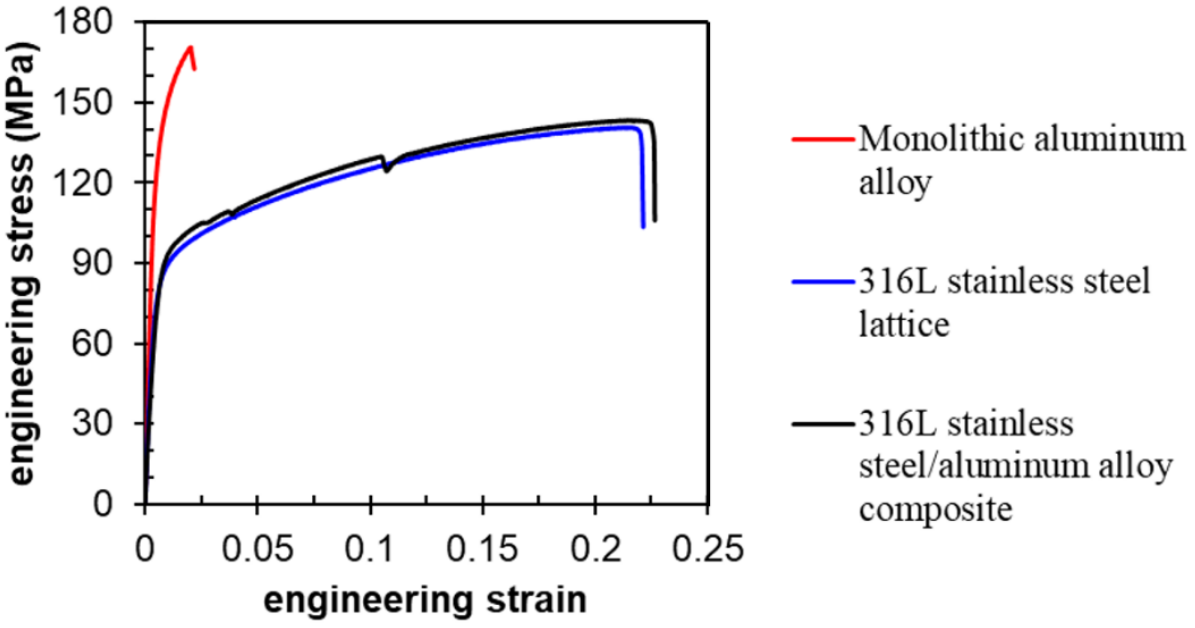

Fig. 5. Representative tensile plots for all experimental materials.

The 316L stainless steel/aluminum composite with the stainless steel volume fraction of 28.8 % in this study exhibited a UTS of 149 MPa and elongation of 22 % (see Table 3). A 316L stainless steel/aluminum composite with the stainless volume fraction of 30 % was reported to have a UTS of 58 MPa and elongation of 4 % [51]. The difference in the UTS can be explained by the difference in the stress calculation, where the average cross sectional area of the stainless steel lattice was used in this study. By taking the cross sectional area of the composite specimen, the UTS value is calculated to be 51 MPa, which is comparable with the UTS reported for the 30 % composite [51]. The significantly higher elongation of the 28.8 vol. % stainless steel composite in this study compared with the 30 vol. % stainless steel composite in the literature can be attributed to the difference in lattice design (diamond vs BCC), SLM parameters, and casting parameters.

For the composite specimen in the present study, the energy to failure per unit volume was calculated by integrating the area under the tensile curve to be 24.7 MJ/m^3, which is dramatically greater than 4.4 MJ/m^3 reported for the 30 vol. % stainless steel composite [51].

Table 3. Tensile properties of the experimental materials. For comparison, tensile characteristics of a bulk 316L stainless steel fabricated by SLM [48] are also listed.

Material	Yield Stress (MPa)	Elastic Modulus (GPa)	Ultimate Tensile Strength (MPa)	Elongation (%)	Work Hardening Coefficient
Bulk 316L stainless steel [48]	539	208	644	43	0.33
316L stainless steel lattice	84	21	147	22	0.30
316L stainless steel/aluminum alloy composite	87	21	149	22	0.31
Monolithic aluminum alloy	125	33	171	2	0.22

3.3. Compressive behavior evaluation

Representative room temperature true stress-true strain curves for compressive behavior of all experimental materials are plotted in Fig. 6. In the case of the monolithic aluminum alloy, the test was stopped prior to the specimen failure because the applied load approached the maximum limit of the load (100 kN) for the mechanical testing machine. For the 316L stainless steel lattice and 316L stainless steel/aluminum alloy composite, however, specimen collapse occurred before the test was stopped. It is evident from Fig. 6 that the yield stress and compressive strength of the monolithic aluminum alloy were noticeably greater than those of the stainless steel lattice and stainless steel/aluminum bimetallic composite. This can be explained by the presence of cavities (Fig. 1) and gaps (Fig. 3) in the microstructure of the lattice and bimetallic composite specimens, respectively. From Fig. 6, it can also be seen that the yield stress and compressive strength of the

stainless steel lattice were significantly lower than those of the bimetallic composite. This contrasts with the observed tensile plots (Fig. 5), where the tensile behavior of both the stainless steel and bimetallic composite was almost the same. This discrepancy can be explained by the orientation of the gaps in the composite material with respect to the loading direction. Whereas the gaps within the stainless steel/aluminum interfaces were closed under the compressive loading, they opened up and propagated under the tensile loading. Thus, the aluminum alloy matrix plays an important role during compressive deformation of the bimetallic composite.

From Fig. 6, the compressive elastic modulus of the monolithic aluminum alloy was determined to be 7.4 GPa. Since this aluminum alloy is a special one, there was not any studies on its compressive properties in the literature. However, the compressive elastic modulus of an as-cast aluminum alloy with a similar composition was reported to be 7.5 GPa [52], which is very similar to the 7.4 GPa measured in the present study. In the case of bulk (nonporous) 316L stainless steel fabricated by SLM, the compressive elastic modulus was reported to be 184 GPa [47]. Using these values and an iso-strain model, the compressive elastic modulus of the bimetallic composite was calculated to be 47.7 GPa. However, the experimental value for the compressive elastic modulus of the bimetallic composite was 7.3 GPa. This discrepancy can be explained by lack of a bond between the stainless steel reinforcement and aluminum alloy matrix in the bimetallic composite. Another explanation can be the strain localization in the weaker aluminum matrix. In fact, the contribution of the reinforcing 316L stainless steel to the bimetallic composite's flow stress is relatively small because it can accommodate large plastic strains under low applied stresses [53]. The compressive elastic modulus of the 316L stainless steel lattice with the diamond design and relative density of 28.8 % was determined to be 7.3 GPa (see Fig. 6). The compressive elastic modulus for an f2cc,z 316L stainless steel lattice with a relative density of 33 % was reported to

be 10.3 GPa [47]. Moreover, Zhong et al. [54] measured the compressive elastic modulus for a tetrakaidecahedron 316L stainless steel lattice with a relative density of 40.4 % to be 1.81 GPa. The difference in compressive elastic modulus can be attributed to the difference in the lattice design, relative density, and SLM process parameters.

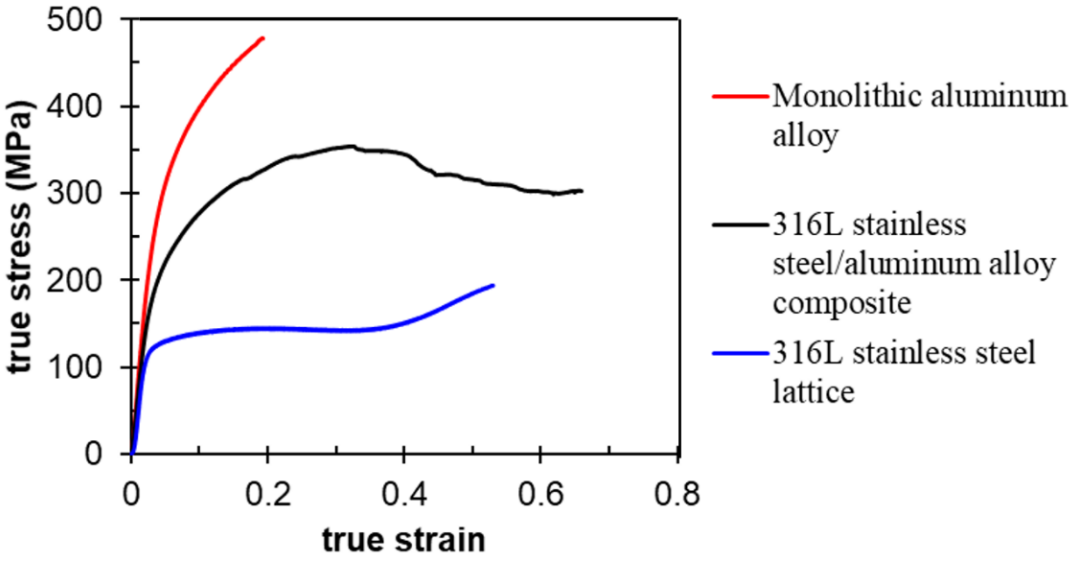

Fig. 6. Representative compressive plots for all experimental materials.

Further inspection of Fig. 6 reveals that the compressive curve of the 316L stainless steel lattice comprised three distinct deformation stages: elastic, plateau, and densification. The initial stage is the elastic deformation which is followed by struts yield. Upon yield point, the plateau plastic deformation stage starts, during which plastic hinges are created at the nodes of the struts. Finally, the lattice enters the densification stage, in which most struts break and are forced to contact each other resulting in a sharp stress rise. This behavior is consistent with schematic stress-strain plot for compressive behavior of foams [55]. The plateau stage is an important characteristic of lattice structures during compressive deformation, which exhibits various features depending on the types of material. Ductile materials exhibit long plateaus without large stress drops, whereas brittle

materials show plateaus with dramatic stress drops [56]. The long plateau region without stress drops observed in Fig. 6 benefits from the excellent ductility of the 316L stainless steel and is significantly different from those of brittle materials such as magnesium alloys whose plateau deformation region exhibit sharp stress drops [57]. Loading response of lattice structures can be either stretch-dominated or bending-dominated [55]. The stretch-dominated lattices have a higher stiffness and strength but lower energy absorption than the bending-dominated lattices. Comparison of the stress-strain curve of the 316L stainless steel lattice (Fig. 6) with the schematic compression stress-strain curves in literature [55, 58] revealed that the diamond 316L stainless steel lattice deformed in a bending-dominated mode. This makes sense considering the higher absorption energy but lower strength of the diamond lattice in the present study compared with the stretch-dominated f2cc,z lattice [47] as discussed above.

3.4. Fracture analysis

An image of all experimental specimens after the tensile testing is shown in Fig. 7. The 316L stainless steel lattice failed by a single fracture at the center of the gauge zone. This indicates that the addition of the fillets to the grip/gauge interfaces (Fig. 1(c)) prevented the fracture in this area. The failure location for the lattice specimen corresponded to the nodes (Fig. 7(a)), where the minimum cross-sectional area existed. This is not surprising considering the presence of the greatest stress concentrations in the nodes. Failure at the nodes was also observed for SLM fabricated Ti-6Al-4V [59] and AlSi10Mg [60] lattice structures. In the case of the 316L stainless steel/aluminum composite (Fig. 7(b)), multiple failure locations were observed along the gauge zone. Moreover, many gaps can be seen in the stainless steel/aluminum interfaces, whose size increases when moving from the gauge ends towards the gauge center. Detachment of the stainless steel reinforcement from the aluminum matrix is evident from Fig. 7(b). It seems that the gaps in

the stainless steel/aluminum interfaces of the as built bimetallic composite (see Fig. 3) opened up during the tensile testing leading to the detachment. The breakage in the stainless steel lattice of the composite material can also be seen in Fig. 7(b). Similar to the lattice specimen, the breakage occurred in the nodes. For the monolithic aluminum alloy, the failure did not occur at the center of the gauge zone (Fig. 7(c)). However, the failure location is still within the gauge zone indicating that the tensile results for this specimen were reliable.

Fig. 7. The experimental samples after the tensile tests: (a) 316L stainless steel lattice; (b) 316L stainless steel/aluminum composite; (c) monolithic aluminum alloy.

In order to observe features presented in the damage zone and identify the main damage mode for all experimental materials, the fracture surfaces were examined after tensile testing to failure. Fig. 8 illustrates SEM micrographs from the fracture surface of the 316L stainless steel lattice specimen at different magnifications. It can be seen that the fracture of the lattice specimen took place at the nodes perpendicular to the tensile direction (Fig. 8(a)), where maximum stress concentrations were located. At higher magnifications (Fig. 8(b,c)), fine dimples, micro-voids, micro-cracks, and cup-cone features were observed with no cleavage facets being observed. Thus, the fracture behavior

of the lattice specimen can be determined to be ductile. The micrometric size of the dimples on the fracture surface corresponds to the micrometric size of the cells in the solidification structure of the SLM-fabricated 316L stainless steel [17, 47]. For the 316L stainless steel parts fabricated by conventional techniques, the dimple size was reported to be significantly larger (up to 20 microns) [61]. The micro-voids and micro-cracks on the fracture surface (see Fig. 8(c)) seem to be the initiation sites for the lattice specimen damage. During the tensile deformation, growth and coalescence of these discontinuities lead to the material failure.

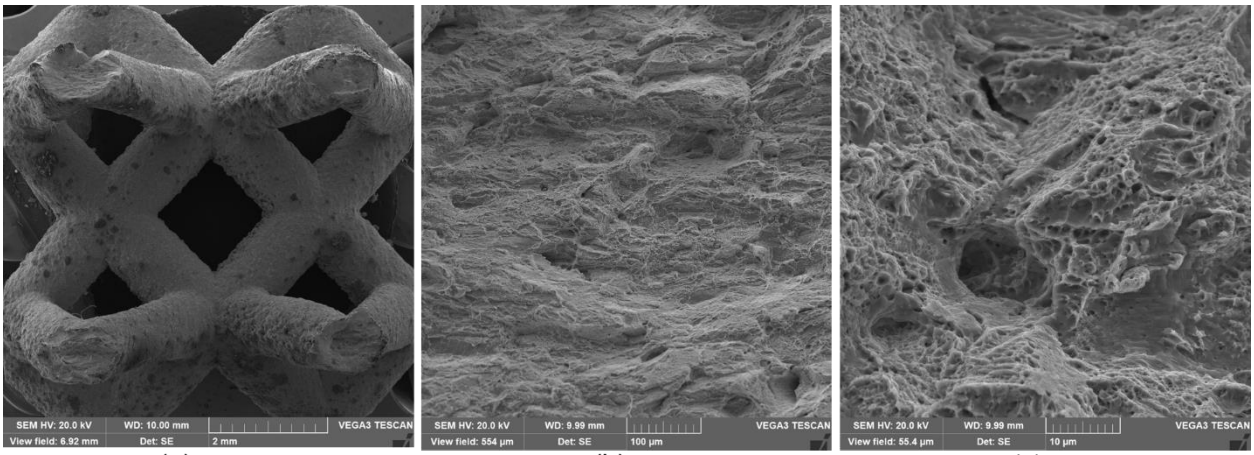

Fig. 8. SEM micrographs from fracture surface of the 316L stainless steel lattice after the tensile testing: (a) low magnification; (b) and (c) high magnification.

SEM micrographs from the fracture surface of the 316L stainless steel lattice/aluminum alloy bimetallic composite at different magnifications are illustrated in Fig. 9. At low magnification (Fig. 9(a)), it can be observed the stainless steel lattice detached from the aluminum alloy matrix. It seems that the narrow gap in the stainless steel/aluminum interfaces (see Fig. 3) opened up during the tensile deformation of the bimetallic composite leading to the wide gap between the stainless steel lattice and aluminum alloy shown in Fig. 9(a). It can also be seen that the fracture of the reinforcing stainless steel lattice took place in the nodes, which is consistent with the

fractograph of the stainless steel lattice specimen depicted in Fig. 8(a). At high magnification (Fig. 9(b)), micro-cracks and cleavage facets were observed on the fracture surface of the aluminum alloy matrix. Thus, the fracture mode of the aluminum alloy matrix can be determined to be brittle. Since the elongation of the bimetallic composite was as large as that of the lattice specimen (Fig. 5 and Table 3), it can be concluded that the aluminum matrix did not play an important role in the fracture behavior of the bimetallic composite. In the case of the stainless steel reinforcement (Fig. 9(c)), the fracture surface mainly comprised fine dimples, micro-voids, micro-cracks, and cup-cone features with no cleavage facets. Thus, the fracture behavior of the lattice reinforcement can be determined to be ductile. Given the relatively large elongation (22 %) of the bimetallic composite, the fracture mode of this specimen can be concluded to be ductile. This means that the fracture mode of the bimetallic composite was dominated by the stainless steel reinforcement.

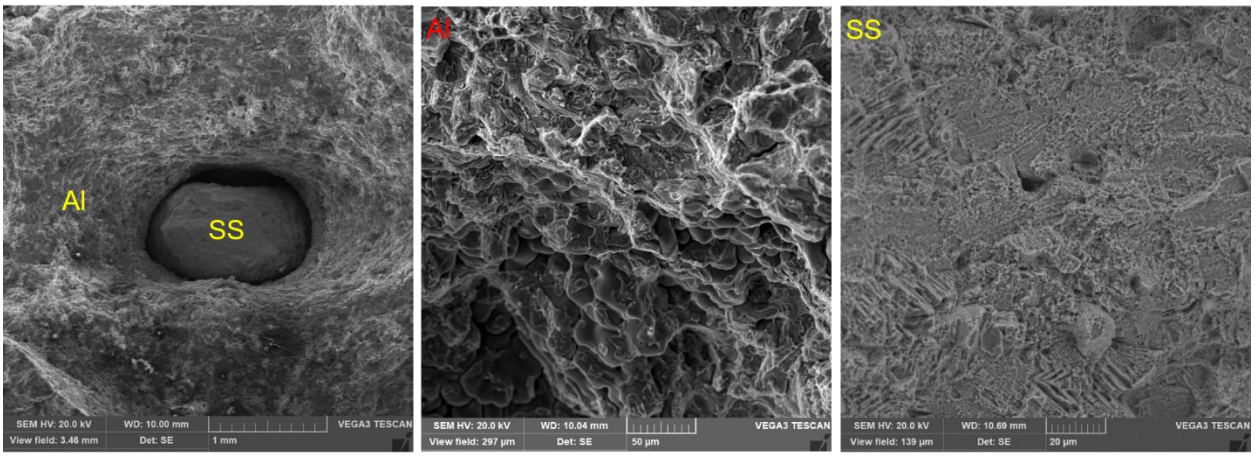

(a) (b) (c)

Fig. 9. SEM micrographs from fracture surface of the 316L stainless steel lattice/aluminum alloy bimetallic composite after the tensile testing: (a) low magnification; (b) and (c) high magnification.

Fractography results for the monolithic aluminum alloy are shown in Fig. 10. The fracture surface of this specimen displayed micro-voids, micro-cracks, a relatively large area fraction of cleavage facets, and some dimples. Thus, the fracture mode of the monolithic aluminum alloy can be

concluded to be brittle. As stated above, a significant amount of porosity (6.4 vol. %) was present in the as-cast monolithic aluminum alloy. These pores quickly open and propagate during the tensile test leading to the brittle fracture. This explains the relatively low elongation (2 %) observed for this material (see Fig. 5 and Table 3). The brittle fracture was already reported for various as-cast aluminum alloys including Al-12Zn-3Mg-2.5Cu [62], 7050 [63], Al-30Si [64], 319 [65], and A356 [66].

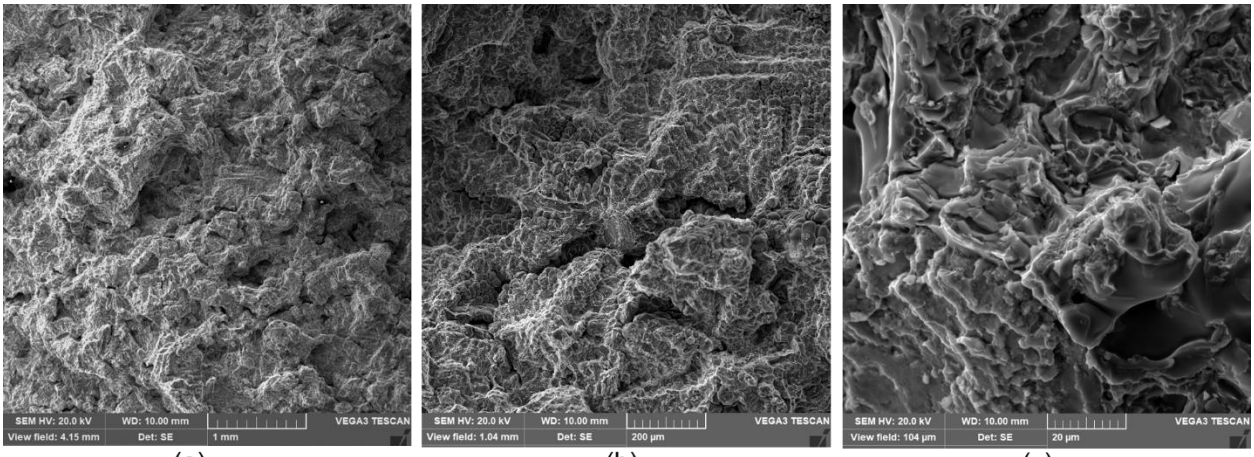

Fig. 10. SEM micrographs from fracture surface of the monolithic aluminum alloy after the tensile testing at different magnifications.

4. Conclusions

This paper provides an original an innovative approach for fabricating bimetallic composites of 316L stainless steel and an aluminum alloy fabricated through a hybrid manufacturing process comprising laser powder bed fusion and vacuum assisted casting. The process results into a near net shape parts with complex bimetallic lattice and matrix structure composed of different materials. By investigating microstructure, mechanical properties, and fracture behavior of 316L

stainless steel lattice, monolithic aluminum alloy, and 316L stainless steel/aluminum alloy bimetallic composite, the following can be concluded:

1) EDS analysis revealed a uniform distribution of the alloying elements in the stainless steel reinforcement of the bimetallic composite. In the case of the aluminum matrix, however, segregation of the alloying elements in grain boundaries was observed.
2) The SLM fabricated 316L stainless steel lattice with the diamond design deformed in a bending-dominated mode. This deformation mode led the lattice displaying a higher absorption energy but a lower tensile strength than the stretch dominated stainless steel lattices with a similar relative density.
3) SEM revealed continuous gaps in the 316L stainless steel/aluminum alloy interfaces of the bimetallic composite. The gaps prevented the load transfer from the stainless steel lattice to the aluminum matrix during tension leading to the bimetallic material exhibiting tensile properties (yield stress, UTS, and elongation) similar to those of the stainless steel lattice.
4) The monolithic aluminum alloy displayed a noticeably higher elastic modulus, yield stress and ultimate tensile strength but a dramatically lower elongation than both the lattice and bimetallic composite materials.
5) The compressive properties of the bimetallic composite were found to be significantly greater than those of the stainless steel lattice. This indicates that the aluminum alloy matrix plays an important role during compressive deformation of the bimetallic composite.
6) Detachment of the stainless steel lattice from the aluminum matrix was determined to be the root cause of failure for the bimetallic composite. Moreover, the fracture mode of both the stainless steel lattice and bimetallic composite was found to be ductile. For the monolithic aluminum alloy, however, the fracture behavior was determined to be brittle.

Declaration of Competing Interest

The authors declare that they have no known competing financial interests that could have appeared to affect the research reported in this paper.

Acknowledgements

The authors acknowledge the Natural Sciences and Engineering Research Council of Canada (NSERC), Alberta Innovates, and Boss Completions Ltd for their financial support. The authors also thank Mr. Kelsey Kalinski from Boss Completions Ltd for valuable discussions.

References

1. Yap, C.Y., Chua, C.K., Dong, Z.L., Liu, Z.H., Zhang, D.Q., Loh, L.E., Sing, S.L.: Review of selective laser melting: Materials and applications. Appl. Phys. Rev. 2, (2015). https://doi.org/10.1063/1.4935926

2. Khaing, M.W., Fuh, J.Y.H., Lu, L.: Direct metal laser sintering for rapid tooling: Processing and characterisation of EOS parts. J. Mater. Process. Technol. 113, 269–272 (2001). https://doi.org/10.1016/S0924-0136(01)00584-2

3. Körner, C.: Additive manufacturing of metallic components by selective electron beam melting - A review. Int. Mater. Rev. 61, 361–377 (2016). https://doi.org/10.1080/09506608.2016.1176289

4. Das, S.: Physical Aspects of Process Control in Selective Laser Sintering of Metals. Adv. Eng. Mater. 5, 701–711 (2003). https://doi.org/10.1002/adem.200310099

5. De Pasquale, G., Luceri, F., Riccio, M.: Experimental Characterization of SLM and EBM Cubic Lattice Structures for Lightweight Applications. Exp. Mech. 59, 469–482 (2019). https://doi.org/10.1007/s11340-019-00481-8

6. Strano, G., Hao, L., Everson, R.M., Evans, K.E.: Surface roughness analysis, modelling and prediction in selective laser melting. J. Mater. Process. Technol. 213, 589–597 (2013). https://doi.org/10.1016/j.jmatprotec.2012.11.011

7. Refai, K., Brugger, C., Montemurro, M., Saintier, N.: An experimental and numerical study of the high cycle multiaxial fatigue strength of titanium lattice structures produced by Selective Laser Melting (SLM). Int. J. Fatigue. 138, 105623 (2020). https://doi.org/10.1016/j.ijfatigue.2020.105623

8. Fan, H., Yang, S.: Effects of direct aging on near-alpha Ti–6Al–2Sn–4Zr–2Mo (Ti-6242) titanium alloy fabricated by selective laser melting (SLM). Mater. Sci. Eng. A. 788, 139533 (2020). https://doi.org/10.1016/j.msea.2020.139533

9. Otani, Y., Sasaki, S.: Effects of the addition of silicon to 7075 aluminum alloy on microstructure, mechanical properties, and selective laser melting processability. Mater. Sci. Eng. A. 777, 139079 (2020). https://doi.org/10.1016/j.msea.2020.139079

10. Ghasri-Khouzani, M., Peng, H., Attardo, R., Ostiguy, P., Neidig, J., Billo, R., Hoelzle, D., Shankar, M.R.: Comparing microstructure and hardness of direct metal laser sintered AlSi10Mg alloy between different planes. J. Manuf. Process. 37, 274–280 (2019). https://doi.org/10.1016/j.jmapro.2018.12.005

11. Zhang, H., Gu, D., Yang, J., Dai, D., Zhao, T., Hong, C., Gasser, A., Poprawe, R.: Selective laser melting of rare earth element Sc modified aluminum alloy: Thermodynamics of precipitation behavior and its influence on mechanical properties. Addit. Manuf. 23, 1–12 (2018). https://doi.org/10.1016/j.addma.2018.07.002

12. Grange, D., Bartout, J.D., Macquaire, B., Colin, C.: Processing a non-weldable nickel-base superalloy by Selective Laser Melting: role of the shape and size of the melt pools on solidification cracking. Materialia. 12, (2020). https://doi.org/10.1016/j.mtla.2020.100686

13. Ivanov, D., Travyanov, A., Petrovskiy, P., Cheverikin, V., Alekseeva, Khvan, A., Logachev, I.: Evolution of structure and properties of the nickel-based alloy EP718 after the SLM growth and after different types of heat and mechanical treatment. Addit. Manuf. 18, 269–275 (2017). https://doi.org/10.1016/j.addma.2017.10.015

14. Rupal, B.S., Anwer, N., Secanell, M., Qureshi, A.J.: Geometric tolerance and manufacturing assemblability estimation of metal additive manufacturing (AM) processes. Mater. Des. 194, 108842 (2020). https://doi.org/10.1016/j.matdes.2020.108842

15. Yin, S., Chen, C., Yan, X., Feng, X., Jenkins, R., O'Reilly, P., Liu, M., Li, H., Lupoi, R.: The influence of aging temperature and aging time on the mechanical and tribological properties of selective laser melted maraging 18Ni-300 steel. Addit. Manuf. 22, 592–600 (2018). https://doi.org/10.1016/j.addma.2018.06.005

16. Seede, R., Shoukr, D., Zhang, B., Whitt, A., Gibbons, S., Flater, P., Elwany, A., Arroyave, R., Karaman, I.: An ultra-high strength martensitic steel fabricated using selective laser melting additive manufacturing: Densification, microstructure, and mechanical properties. Acta Mater. 186, 199–214 (2020). https://doi.org/10.1016/j.actamat.2019.12.037

17. Ghasri-Khouzani, M., Peng, H., Attardo, R., Ostiguy, P., Neidig, J., Billo, R., Hoelzle, D., Shankar, M.R.: Direct metal laser-sintered stainless steel: comparison of microstructure and hardness between different planes. Int. J. Adv. Manuf. Technol. 95, 4031–4037 (2018). https://doi.org/10.1007/s00170-017-1528-y

18. Dilip, J.J.S., Ram, G.D.J., Starr, T.L., Stucker, B.: Selective laser melting of HY100 steel: Process parameters, microstructure and mechanical properties. Addit. Manuf. 13, 49–60 (2017). https://doi.org/10.1016/j.addma.2016.11.003

19. Boes, J., Röttger, A., Mutke, C., Escher, C., Theisen, W.: Microstructure and mechanical properties of X65MoCrWV3-2 cold-work tool steel produced by selective laser melting. Addit. Manuf. 23, 170–180 (2018). https://doi.org/10.1016/j.addma.2018.08.005

20. Abbasi, M., Karimi Taheri, A., Salehi, M.T.: Growth rate of intermetallic compounds in Al/Cu bimetal produced by cold roll welding process. J. Alloys Compd. 319, 233–241 (2001). https://doi.org/10.1016/S0925-8388(01)00872-6

21. Zareie Rajani, H.R., Akbari Mousavi, S.A.A.: The effect of explosive welding parameters on metallurgical and mechanical interfacial features of Inconel 625/plain carbon steel bimetal plate. Mater. Sci. Eng. A. 556, 454–464 (2012). https://doi.org/10.1016/j.msea.2012.07.012

22. Yao, C., Xu, B., Zhang, X., Huang, J., Fu, J., Wu, Y.: Interface microstructure and mechanical properties of laser welding copper-steel dissimilar joint. Opt. Lasers Eng. 47, 807–814 (2009). https://doi.org/10.1016/j.optlaseng.2009.02.004

23. Viala, J.C., Peronnet, M., Barbeau, F., Bosselet, F., Bouix, J.: Interface chemistry in aluminium alloy castings reinforced with iron base inserts. Compos. Part A Appl. Sci. Manuf. 33, 1417–1420 (2002). https://doi.org/10.1016/S1359-835X(02)00158-6

24. Vendra, L.J., Rabiei, A.: A study on aluminum-steel composite metal foam processed by casting. Mater. Sci. Eng. A. 465, 59–67 (2007). https://doi.org/10.1016/j.msea.2007.04.037

25. Anderson, R., Terrell, J., Schneider, J., Thompson, S., Gradl, P.: Characteristics of Bi-metallic Interfaces Formed During Direct Energy Deposition Additive Manufacturing Processing. Metall. Mater. Trans. B Process Metall. Mater. Process. Sci. 50, 1921–1930 (2019). https://doi.org/10.1007/s11663-019-01612-1

26. Onuike, B., Bandyopadhyay, A.: Functional bimetallic joints of Ti6Al4V to SS410. Addit. Manuf. 31, 100931 (2020). https://doi.org/10.1016/j.addma.2019.100931

27. Sahasrabudhe, H., Harrison, R., Carpenter, C., Bandyopadhyay, A.: Stainless steel to titanium bimetallic structure using LENS^{TM}. Addit. Manuf. 5, 1–8 (2015). https://doi.org/10.1016/j.addma.2014.10.002

28. Zhang, X., Sun, C., Pan, T., Flood, A., Zhang, Y., Li, L., Liou, F.: Additive manufacturing of copper – H13 tool steel bi-metallic structures via Ni-based multi-interlayer. Addit. Manuf. 36, 101474 (2020). https://doi.org/10.1016/j.addma.2020.101474

29. Banait, S.M., Paul, C.P., Jinoop, A.N., Kumar, H., Pawade, R.S., Bindra, K.S.: Experimental investigation on laser directed energy deposition of functionally graded layers of Ni-Cr-B-Si and SS316L. Opt. Laser Technol. 121, 105787 (2020). https://doi.org/10.1016/j.optlastec.2019.105787

30. Liu, Z.H., Zhang, D.Q., Sing, S.L., Chua, C.K., Loh, L.E.: Interfacial characterization of SLM parts in multi-material processing: Metallurgical diffusion between 316L stainless steel and C18400 copper alloy. Mater. Charact. 94, 116–125 (2014). https://doi.org/10.1016/j.matchar.2014.05.001

31. Demir, A.G., Previtali, B.: Multi-material selective laser melting of Fe/Al-12Si components. Manuf. Lett. 11, 8–11 (2017). https://doi.org/10.1016/j.mfglet.2017.01.002

32. Mei, X., Wang, X., Peng, Y., Gu, H., Zhong, G., Yang, S.: Interfacial characterization and mechanical properties of 316L stainless steel/inconel 718 manufactured by selective laser melting. Mater. Sci. Eng. A. 758, 185–191 (2019). https://doi.org/10.1016/j.msea.2019.05.011

33. Tey, C.F., Tan, X., Sing, S.L., Yeong, W.Y.: Additive manufacturing of multiple materials by selective laser melting: Ti-alloy to stainless steel via a Cu-alloy interlayer. Addit. Manuf. 31, 100970 (2020). https://doi.org/10.1016/j.addma.2019.100970

34. Gradl, P.R., Protz, C.S., Ellis, D.L., Greene, S.E.: Progress in additively manufactured copper-alloy GRCOP-84, GRCOP-42, and bimetallic combustion chambers for liquid rocket engines. Proc. Int. Astronaut. Congr. IAC. 2019-Octob, 21–25 (2019)

35. Onuike, B., Heer, B., Bandyopadhyay, A.: Additive manufacturing of Inconel 718—Copper alloy bimetallic structure using laser engineered net shaping (LENS^{TM}). Addit. Manuf. 21, 133–140 (2018). https://doi.org/10.1016/j.addma.2018.02.007

36. Fan, H.L., Fang, D.N., Jing, F.N.: Yield surfaces and micro-failure mechanism of block lattice truss materials. Mater. Des. 29, 2038–2042 (2008). https://doi.org/10.1016/j.matdes.2008.04.013

37. ASTM E8: ASTM E8/E8M standard test methods for tension testing of metallic materials 1. Annu. B. ASTM Stand. 4. 1–27 (2010). https://doi.org/10.1520/E0008

38. Jiang, W., Li, G., Wu, Y., Liu, X., Fan, Z.: Effect of heat treatment on bonding strength of aluminum/steel bimetal produced by a compound casting. J. Mater. Process. Technol. 258, 239–250 (2018). https://doi.org/10.1016/j.jmatprotec.2018.04.006

39. Pauly, S., Wang, P., Kühn, U., Kosiba, K.: Experimental determination of cooling rates in selectively laser-melted eutectic Al-33Cu. Addit. Manuf. 22, 753–757 (2018). https://doi.org/10.1016/j.addma.2018.05.034

40. Alnajjar, M., Christien, F., Wolski, K., Bosch, C.: Evidence of austenite by-passing in a stainless steel obtained from laser melting additive manufacturing. Addit. Manuf. 25, 187–195 (2019). https://doi.org/10.1016/j.addma.2018.11.004

41. Jahangiri, A., Marashi, S.P.H., Mohammadaliha, M., Ashofte, V.: The effect of pressure and pouring temperature on the porosity, microstructure, hardness and yield stress of AA2024 aluminum alloy during the squeeze casting process. J. Mater. Process. Technol. 245, 1–6 (2017). https://doi.org/10.1016/j.jmatprotec.2017.02.005

42. Xu, H., Jian, X., Meek, T.T., Han, Q.: Degassing of molten aluminum A356 alloy using ultrasonic vibration. Mater. Lett. 58, 3669–3673 (2004). https://doi.org/10.1016/j.matlet.2004.02.055

43. Talebian, M., Alizadeh, M.: Manufacturing Al/steel multilayered composite by accumulative roll bonding and the effects of subsequent annealing on the microstructural and mechanical characteristics. Mater. Sci. Eng. A. 590, 186–193 (2014). https://doi.org/10.1016/j.msea.2013.10.026

44. Liu, J., Jiang, S., Shi, Y., Kuang, Y., Huang, G., Zhang, H.: Laser fusion-brazing of aluminum alloy to galvanized steel with pure Al filler powder. Opt. Laser Technol. 66, 1–8 (2015). https://doi.org/10.1016/j.optlastec.2014.08.004

45. Watanabe, T., Takayama, H., Yanagisawa, A.: Joining of aluminum alloy to steel by friction stir welding. J. Mater. Process. Technol. 178, 342–349 (2006). https://doi.org/10.1016/j.jmatprotec.2006.04.117

46. Acarer, M., Demir, B.: An investigation of mechanical and metallurgical properties of explosive welded aluminum-dual phase steel. Mater. Lett. 62, 4158–4160 (2008). https://doi.org/10.1016/j.matlet.2008.05.060

47. Köhnen, P., Haase, C., Bültmann, J., Ziegler, S., Schleifenbaum, J.H., Bleck, W.: Mechanical properties and deformation behavior of additively manufactured lattice structures of stainless steel. Mater. Des. 145, 205–217 (2018). https://doi.org/10.1016/j.matdes.2018.02.062

48. Hitzler, L., Hirsch, J., Heine, B., Merkel, M., Hall, W., Ochsner, A.: On the Anisotropic Mechanical Properties of Selective-Laser Melted Stainless Steel. Maters. 10, 1136 (2017). https://doi.org/10.3390/ma10101136

49. Shamsujjoha, M., Agnew, S.R., Fitz-Gerald, J.M., Moore, W.R., Newman, T.A.: High Strength and Ductility of Additively Manufactured 316L Stainless Steel Explained. Metall. Mater. Trans. A Phys. Metall. Mater. Sci. 49, 3011–3027 (2018). https://doi.org/10.1007/s11661-018-4607-2

50. Vorozhtsov, S.A., Khrustalyov, P., Eskin, D.G., Kulkov, S.N., Alba-Baena, N.: The Physical-Mechanical and Electrical Properties of Cast Aluminum-Based Alloys Reinforced with Diamond Nanoparticles. Russ. Phys. J. 57, 1485–1490 (2015). https://doi.org/10.1007/s11182-015-0412-1

51. Cheng, J., Gussev, M., Allen, J., Hu, X., Moustafa, A.R., Splitter, D.A., Shyam, A.: Deformation and failure of PrintCast A356/316 L composites: Digital image correlation and finite element modeling. Mater. Des. 195, 109061 (2020). https://doi.org/10.1016/j.matdes.2020.109061

52. Azadi, M., Zolfaghari, M., Rezanezhad, S., Azadi, M.: Effects of SiO2 nano-particles on tribological and mechanical properties of aluminum matrix composites by different dispersion methods. Appl. Phys. A Mater. Sci. Process. 124, 1–13 (2018). https://doi.org/10.1007/s00339-018-1797-9

53. Smith, M., Guan, Z., Cantwell, W.J.: Finite element modelling of the compressive response of lattice structures manufactured using the selective laser melting technique. Int. J. Mech. Sci. 67, 28–41 (2013). https://doi.org/10.1016/j.ijmecsci.2012.12.004

54. Zhong, T., He, K., Li, H., Yang, L.: Mechanical properties of lightweight 316L stainless steel lattice structures fabricated by selective laser melting. Mater. Des. 181, 108076 (2019). https://doi.org/10.1016/j.matdes.2019.108076

55. Gibson, Lorna J., and M.F.A.: Cellular solids: structure and properties. Cambridge University Press (1999)

56. Maskery, I., Aboulkhair, N.T., Aremu, A.O., Tuck, C.J., Ashcroft, I.A., Wildman, R.D., Hague, R.J.M.: A mechanical property evaluation of graded density Al-Si10-Mg lattice structures manufactured by selective laser melting. Mater. Sci. Eng. A. 670, 264–274 (2016). https://doi.org/10.1016/j.msea.2016.06.013

57. Hong, K., Park, H., Kim, Y., Knapek, M., Minárik, P., Máthis, K., Yamamoto, A., Choe, H.: Mechanical and biocorrosive properties of magnesium-aluminum alloy scaffold for biomedical applications. J. Mech. Behav. Biomed. Mater. 98, 213–224 (2019). https://doi.org/10.1016/j.jmbbm.2019.06.022

58. Rashed, M.G., Ashraf, M., Mines, R.A.W., Hazell, P.J.: Metallic microlattice materials: A current state of the art on manufacturing, mechanical properties and applications. Mater. Des. 95, 518–533 (2016). https://doi.org/10.1016/j.matdes.2016.01.146

59. Soro, N., Saintier, N., Merzeau, J., Veidt, M., Dargusch, M.S.: Quasi-static and fatigue properties of graded Ti–6Al–4V lattices produced by Laser Powder Bed Fusion (LPBF). Addit. Manuf. 101653 (2020). https://doi.org/10.1016/j.addma.2020.101653

60. Suzuki, A., Sekizawa, K., Liu, M., Takata, N., Kobashi, M.: Effects of Heat Treatments on Compressive Deformation Behaviors of Lattice-Structured AlSi10Mg Alloy Fabricated by

Selective Laser Melting. Adv. Eng. Mater. 21, 1–9 (2019). https://doi.org/10.1002/adem.201900571

61. Matsuo, T., Yamabe, J., Matsuoka, S.: Effects of hydrogen on tensile properties and fracture surface morphologies of Type 316L stainless steel. Int. J. Hydrogen Energy. 39, 3542–3551 (2014). https://doi.org/10.1016/j.ijhydene.2013.12.099

62. Pourkia, N., Emamy, M., Farhangi, H., Ebrahimi, S.H.S.: The effect of Ti and Zr elements and cooling rate on the microstructure and tensile properties of a new developed super high-strength aluminum alloy. Mater. Sci. Eng. A. 527, 5318–5325 (2010). https://doi.org/10.1016/j.msea.2010.05.009

63. Lalpoor, M., Eskin, D.G., ten Brink, G., Katgerman, L.: Microstructural features of intergranular brittle fracture and cold cracking in high strength aluminum alloys. Mater. Sci. Eng. A. 527, 1828–1834 (2010). https://doi.org/10.1016/j.msea.2009.11.003

64. Rao, A.G., Deshmukh, V.P., Prabhu, N., Kashyap, B.P.: Ductilizing of a brittle as-cast hypereutectic Al-Si alloy by friction stir processing. Mater. Lett. 159, 417–419 (2015). https://doi.org/10.1016/j.matlet.2015.07.006

65. Ma, Z., Samuel, A.M., Doty, H.W., Valtierra, S., Samuel, F.H.: Effect of Fe content on the fracture behaviour of Al-Si-Cu cast alloys. Mater. Des. 57, 366–373 (2014). https://doi.org/10.1016/j.matdes.2014.01.037

66. Casari, D., Ludwig, T.H., Merlin, M., Arnberg, L., Garagnani, G.L.: The effect of Ni and V trace elements on the mechanical properties of A356 aluminium foundry alloy in as-cast

and T6 heat treated conditions. Mater. Sci. Eng. A. 610, 414–426 (2014).

https://doi.org/10.1016/j.msea.2014.05.059